Biomaterials 326 (2026) 123655

Contents lists available at ScienceDirect

Biomaterials

journal homepage: www.elsevier.com/locate/biomaterials

# Tumor-activated nanocomplex reprograms cancer and macrophage metabolism in opposite directions to overcome immune suppression

Zan Dai [a,b,*], Qiaoyun Wang [a,c,**], Ming Zhang [d], Yiru Shi [e], Yannan Yang [e], Hao Song [a], Runming Wang [f], Bernt Johannessen [g], Xu Zhen [h], Chengzhong Yu [a,***]

[a] Australian Institute for Bioengineering and Nanotechnology, The University of Queensland, Brisbane, QLD, 4072, Australia
[b] Children's Cancer Institute, School of Medicine and Health, UNSW Sydney, Sydney, 2052, Australia
[c] School of Chemistry, UNSW Sydney, Sydney, 2052, Australia
[d] School of Chemical Engineering, UNSW Sydney, Sydney, 2052, Australia
[e] South Australian ImmunoGENomics Cancer Institute, Faculty of Health and Medical Sciences, The University of Adelaide, Adelaide, South Australia, 5005, Australia
[f] Institute of Biopharmaceutical and Health Engineering, Shenzhen International Graduate School, Tsinghua University, Shenzhen, China
[g] Australian Synchrotron, Australian Nuclear Science and Technology Organization, Clayton, VIC, 3168, Australia
[h] MOE Key Laboratory of High Performance Polymer Materials & Technology, School of Chemistry& Chemical Engineering, Nanjing University, Nanjing, 210023, China

ARTICLE INFO

*Keywords:*
Nanocomplex
Tumor metabolism
Macrophage
Cancer immunotherapy

ABSTRACT

Immunotherapy efficacy is hindered by the immunosuppressive metabolism of cancer cells and tumor-associated macrophages (TAMs), yet their opposite metabolic programs complicate synchronized modulation of tumor microenvironment. Here, we report an acid-activated Fe–Zn nanocomplex (FZNC) that transforms into spiky FeOOH nanoparticles within the tumor microenvironment. This transformation enhances cellular uptake and enables selective scavenging of hydrogen sulfide ($H_2S$)—a metabolite that promotes glycolysis in cancer cells and oxidative phosphorylation (OXPHOS) in TAMs. Local $H_2S$ depletion by FZNCs induces a bidirectional metabolic shift: cancer cells are redirected from glycolysis to OXPHOS, while TAMs switch from OXPHOS to glycolysis. This dual reprogramming enhances tumor immunogenicity with increased dendritic cell maturation and M1 polarization *in vitro*, and enhanced cytotoxic T-cell infiltration *in vivo*. FZNCs treatment suppresses tumor growth and metastasis, with synergistic effects when combined with PD-L1 blockade. This work introduces a materials-based strategy to spatially coordinate opposing metabolic programs for improved antitumor immunity.

## 1. Introduction

Cancer treatment continues to face significant challenges, with tumor metabolism playing a crucial role in disease progression and immune escape [1,2]. In the tumor microenvironment, cancer cells and tumor-associated macrophages (TAMs) together account for nearly 70–90 % of the cellular composition [3,4]. Interestingly, cancer cells and TAMs adapt opposite metabolic programs that contribute to maintaining an immunosuppressive tumor microenvironment [5,6]. Cancer cells predominantly rely on glycolysis for energy production—a phenomenon known as the Warburg effect [7], while TAMs use oxidative phosphorylation (OXPHOS) to sustain their immunosuppressive phenotype [8]. The metabolic difference between cancer cells and TAMs creates a fundamental biological barrier to simultaneously reprogram both cell types, although this strategy is conceptually attractive. Indeed, extensive studies have shown that metabolic reprogramming of either cancer cells or TAMs alone can enhance antitumor immunity and improve therapeutic outcomes [9–14]. However, how to regulate the opposite metabolic programs in both cell types in parallel remains an unmet challenge.

Hydrogen sulfide ($H_2S$) has been widely studied as a metabolic regulator, its effects varies across different cell types [15–17]. In particular, the impact of $H_2S$ on metabolism differs markedly between cancer cells and macrophages. In cancer cells, $H_2S$ enhances glycolysis through pleiotropic mechanisms, such as reducing the mitochondrial $NAD^+$/NADH ratio and suppressing malate-aspartate shuttling [18,19], thereby supporting rapid energy production for proliferation [20]. In

* Corresponding author. Australian Institute for Bioengineering and Nanotechnology, The University of Queensland, Brisbane, QLD, 4072, Australia.
** Corresponding author. Australian Institute for Bioengineering and Nanotechnology, The University of Queensland, Brisbane, QLD, 4072, Australia.
*** Corresponding author. Australian Institute for Bioengineering and Nanotechnology, The University of Queensland, Brisbane, QLD, 4072, Australia.
*E-mail addresses:* zan.dai@unsw.edu.au, zdai@ccia.rog.au (Z. Dai), qiaoyun.wang@unsw.edu.au (Q. Wang), c.yu@uq.edu.au (C. Yu).

https://doi.org/10.1016/j.biomaterials.2025.123655
Received 22 June 2025; Received in revised form 13 August 2025; Accepted 28 August 2025
Available online 29 August 2025

macrophages, $H_2S$ promotes OXPHOS either by enhancing mitochondrial electron transport or limiting store-operated calcium entry [21,22], which supports TAMs in their anti-inflammatory M2-like phenotype [23]. The differential metabolic effects of $H_2S$ on cancer cells and TAMs, together with the observation of elevated $H_2S$ levels in tumors [24], make $H_2S$ a highly attractive target for therapeutic intervention. However, $H_2S$ also functions as an essential gasotransmitter involved in various physiological processes [25,26], making it difficult to manipulate without inducing systemic side effects. For example, systemic use of cystathionine γ-lyase inhibitors can broadly suppress $H_2S$ production, impairing physiological signaling and causing hepatotoxicity [27–29]. Despite extensive interest, it remains unknown how tumor-specific $H_2S$ depletion might reshape the metabolism of both cancer cells and TAMs simultaneously. This gap raises the need for a tumor-specific strategy to reduce $H_2S$ level within the tumor microenvironment.

To develop dual metabolic regulation of cancer cells and TAMs in tumor microenvironment *via* tumor-selective $H_2S$ depletion, a tumor-activatable Fe–Zn bimetallic nanocomplex (FZNC) is reported in this study based on a bimetallic metal-organic framework (MOF) structure (Scheme 1, part I). The nanocomplex is constructed by coordinating $Fe^{3+}$ and $Zn^{2+}$ ions with 2-methylimidazole (HmIM) as the organic linker, forming a MOF-like architecture. Upon exposure to the acidic tumor microenvironment, FZNCs transform into spiky FeOOH nanoparticles—a sulfur scavenger used in industry [30,31], that has also been reported recently to reduce intratumoral $H_2S$ levels *in vivo* [32]. This transformation brings two significant biological effects (Scheme 1, part II): (1) enhanced cellular uptake due to surface topology, which increases particle–cell membrane interactions and penetrates lysosome membrane [33], and (2) tumor-specific $H_2S$ depletion, in which the *in-situ* formed FeOOH acts as the key reactive species for $H_2S$ oxidation, while the spiky structure promotes its tumor enrichment through enhanced cellular uptake and nanoparticle accumulation. The localized $H_2S$ depletion induces a unique dual-cell metabolic reprogramming (Scheme 1, part III): shifting cancer cell metabolism from glycolysis to OXPHOS, while simultaneously redirecting macrophage metabolism from OXPHOS to glycolysis. This synchronous yet opposite modulation of metabolism significantly enhances the immunogenicity of the tumor microenvironment. In animal models, this metabolic shift leads to increased T-cell infiltration, reduced expression of immunosuppressive markers, suppressed tumor growth and metastasis, and extended survival—especially when combined with immune checkpoint blockade therapy. By reversing the immunosuppressive metabolic landscape, this strategy offers a promising avenue for amplifying the efficacy of existing cancer immunotherapies.

## 2. Results and discussion

The FZNCs were synthesized *via* a one-step reaction at 4 °C, exhibiting a spherical morphology (Fig. 1A and S1) with an approximate size of 130 nm as shown by dynamic light scattering (Fig. S2). The Fe:Zn molar ratio in FNZCs was determined to be 0.8 by using inductively coupled plasma optical emission spectroscopy (ICP-OES) analysis (Table S1). The high-angle annular dark-field transmission electron microscopy (HAADF-STEM) image and corresponding energy-dispersive X-ray spectroscopy (EDS) elemental mapping images (Fig. 1B) demonstrated a uniform distribution of Fe, Zn and N (from HmIM) elements. X-ray diffraction (XRD) pattern of the FZNCs revealed no distinct diffraction peak (Fig. S3), indicating an amorphous nature.

To understand how FZNCs are formed, time-dependent studies were performed for samples prepared at different time points using various techniques. Firstly, the XRD analysis (Fig. 1C) showed diffraction peaks (marked by grey dots) attributed to zeolitic imidazolate framework-8 (ZIF-8) at 5 min of reaction [34], their peak intensity decreased gradually till 30 min. To characterize the structural change with time, the products at 5- and 30-min reaction were examined by Raman spectroscopy. As shown in Fig. 1D, the 5-min product exhibited signals at 168, 685, 1146, and 1460 $cm^{-1}$ assigned to Zn–N stretching, imidazole ring puckering, C5–N stretching, and methyl bending of ZIF-8, respectively [35]. The 30-min product presented similar Raman peaks associated with ZIF-8, but with noticeable peak broadening and splitting (indicated by yellow squares). This observation is different from typical $Fe^{2+}$ doped ZIF-8, [36] suggesting that the coordination of $Fe^{3+}$-N forms at reaction time of 30 min after the initial Zn–N coordination formation in ZIF-8. The time-dependent ICP-OES analysis supports a similar conclusion: negligible Fe was observed in the 5 min product, while the Fe/Zn molar ratio gradually increased from 5 min to 30 min (0.01–0.80, Table S1).

To understand the time-dependent change in coordination chemistry, the pH of the reaction system was monitored over time. As shown in Fig. S4, the system pH was as high as 13.2 at the beginning of reaction, then decreased to below 8 after 5 min of reaction. According to the hard and soft acids and bases (HSAB) principle, $Zn^{2+}$ ions, with lower chemical hardness (10.8) than $Fe^{3+}$ (13.1), preferentially coordinate to deprotonated $mIM^-$ ligands under high alkalinity conditions [37], leading to decrease in pH. Nitrogen adsorption-desorption analysis test

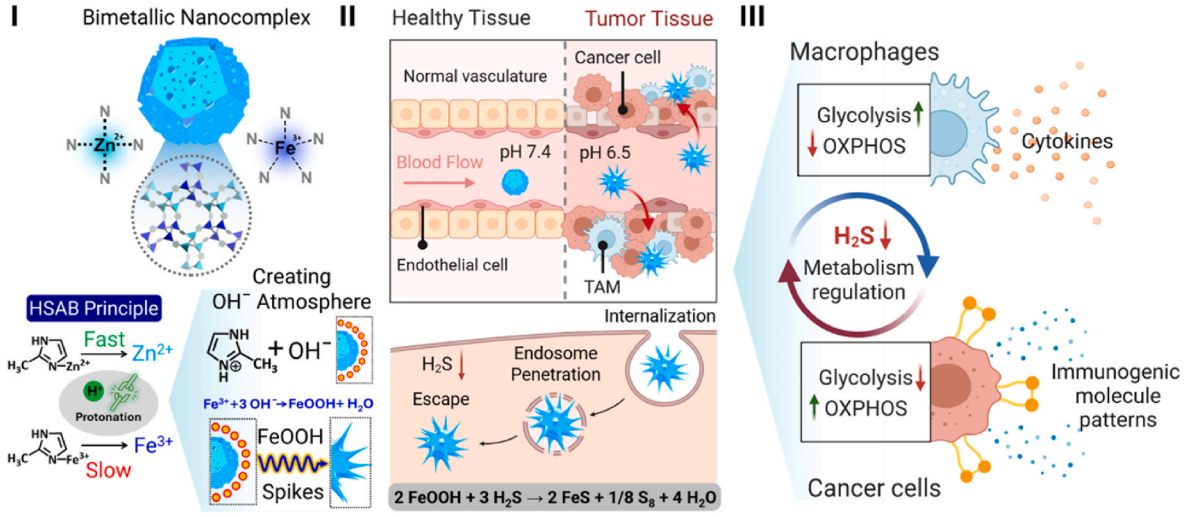


**Scheme 1.** Illustration of tumor-selective $H_2S$ depletion and dual-cell metabolic reprogramming by FZNCs. (I) The structure of FZNCs and its transformation in tumor microenvironment. (II) Tumor-responsive generation of spiky topology for enhanced cellular uptake and endosome escape. (III) Tumor-specific $H_2S$ depletion reprograms cancer and macrophage metabolism in opposite directions.

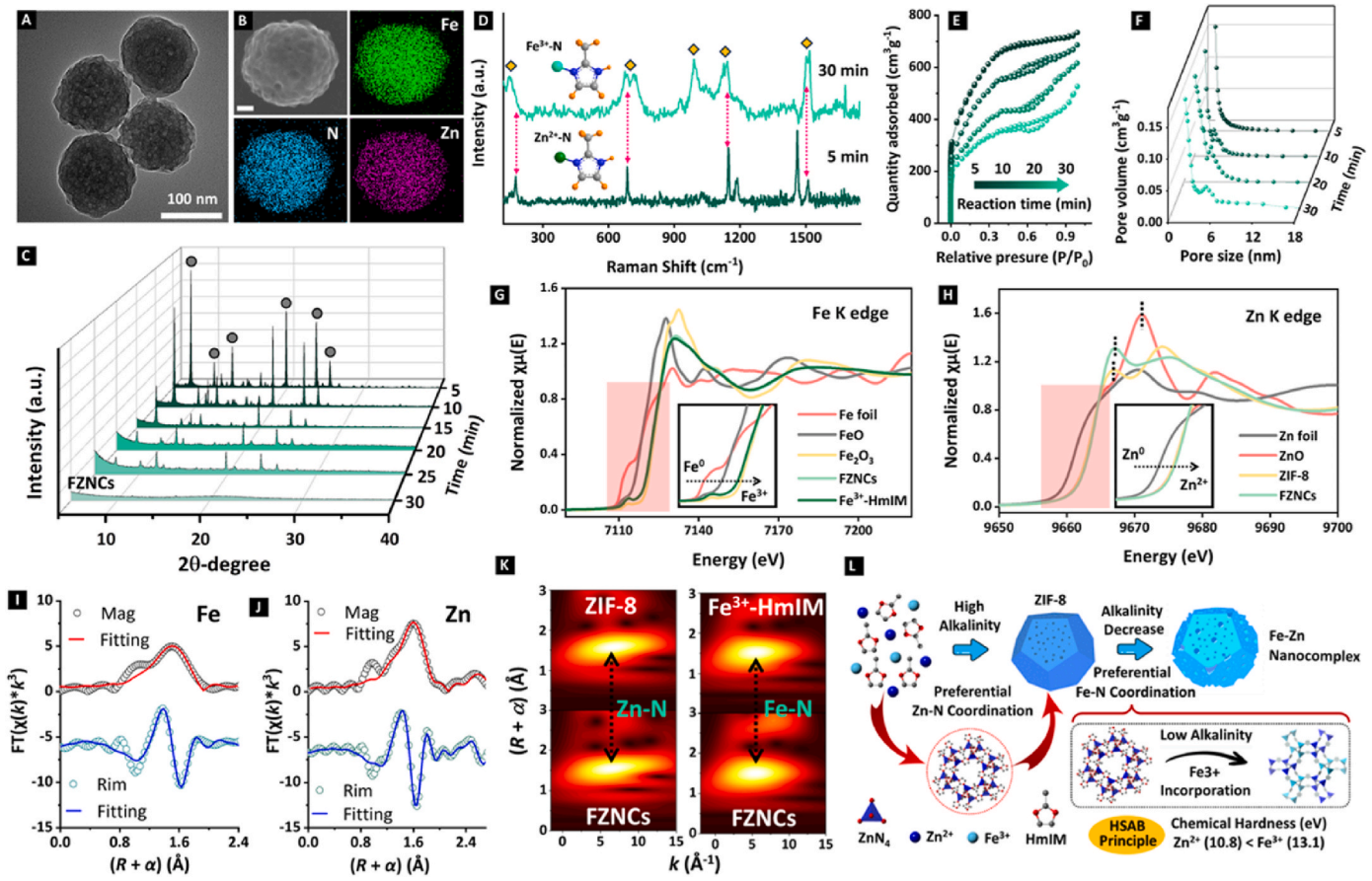


**Fig. 1. Synthesis, structural characterization and formation mechanism of Fe–Zn nanocomplexes (FZNCs).** (A) TEM, (B) HAADF and EDS elemental mapping images of FZNCs. Time dependent (C) XRD patterns, (D) Raman spectra, (E) nitrogen adsorption-desorption isotherms and (F) pore size distribution of FZNCs products obtained from 5 to 30 min. (G–H) XANES spectra at the Fe K-edge and Zn K-edge (inset: the enlarged pre-edges as marked with red colour). (I–J) FT-EXAFS spectra of Fe and Zn in FZNC. (K) WT-EXAFS spectra of ZIF-8, FZNCs and $Fe^{3+}$-HmIM compound. (L) Schematic illustrating the formation mechanism of FZNCs. (For interpretation of the references to color in this figure legend, the reader is referred to the Web version of this article.)

showed a decrease in the BET specific surface area from 1650 to 1179 $m^2/g$ (Fig. 1E) and a corresponding increase in pore size from 1.9 to 4.8 nm (Fig. 1F), as summarized in Table S1. FZNCs are derived from ZIF-8, but compared to ZIF-8, their pores become larger while the specific surface area decreases. This suggests that the intrinsic framework pores of ZIF-8 have collapsed, and FZNCs no longer retain the original ZIF-8 framework structure.

To obtain further insights into the electronic structure and coordination environment in FZNCs, X-ray absorption near-edge structure (XANES) and extended X-ray absorption fine structure (EXAFS) were carried out. As shown in Fig. 1G, Fe K-edge XANES spectra of FZNCs shows an edge energy position very close to $Fe_2O_3$ standard sample and almost the same as the compound of $Fe^{3+}$ and HmIM coordination ($Fe^{3+}$-HmIM, Fig. S5), demonstrating that Fe exists as +3 valence state in FZNCs. The EXAFS fitting results (Fig. 1I and S6) reveal minimal changes in the coordination number for the first shell of the Fe–N path or in bonding distance (Table S2), indicating a Fe coordination environment in FZNCs. Meanwhile, the Zn K-edge XANES spectra of ZIF-8 and FZNCs have similar near-edge absorption energies to ZnO as standard (Fig. 1H), indicating that the valence state of Zn atoms in FZNCs is close to +2. The relatively higher energy of $Zn^{2+}$ in FZNCs compared to ZIF-8 (9667.7 vs 9666.2 eV) indicates partial electron transfer from $Zn^{2+}$ to $Fe^{3+}$ that decreases the electron density around Zn, mainly due to the higher electronegativity of Fe than Zn [38]. The higher partial positive charge density of Zn in FZNCs than in ZIF-8 is consistent with EXAFS fitting results (Fig. 1J and S6), which show an increased coordination number from 4.1 in ZIF-8 to 4.9 in FZNCs (Table S3). In addition, the first shell at around 1.6 Å and 1.5 Å in R-space (Fig. 1K) indicates the Zn–N and Fe–N path in FZNCs, which is similar to that of ZIF-8 and $Fe^{3+}$-HmIM, respectively. Taken together, these findings indicate that the $Fe^{3+}$ coordination not only alters the electronic environment of Zn but also disrupts the original ZIF-8 framework, leading to the formation of a Fe–N/Zn–N co-coordinated structure in FZNCs.

Fig. 1L illustrates the formation mechanism of FZNCs. Initially, under a high alkalinity condition, $Zn^{2+}$ ions (chemical hardness = 10.8) preferentially coordinate with $mIM^-$ ligands with a delocalized negatively charge, forming a typical ZIF-8 structure. As the decreases in alkalinity and $Zn^{2+}$ concentration, $Fe^{3+}$ ions (chemical hardness = 13.1) may coordinate with $mIM^-$ and incorporate into the framework, leading to the formation of a Fe and Zn bimetallic nanocomplex with a disordered structure.

The trivalent Fe and low reaction temperature (4 °C) are crucial for generating the FZNCs. Either divalent Fe or higher temperature failed to yield well-dispersed FZNCs: synthesis with divalent Fe at $N_2$ atmosphere generated a typical ZIF-8 structure (Fig. S7), likely due to formation of $Fe^{2+}$-doped ZIF-8, whereas higher temperatures caused nanoparticles aggregation (Fig. S8), presumably due to faster reaction rates. Therefore, trivalent Fe and a sufficiently low temperature is essential to achieving the stable Fe–Zn bimetallic framework of FZNCs.

We next explored the responsiveness of FZNCs to acidic conditions. After exposing to pH 6.5 for 3 h, the TEM images (Fig. 2A–C) reveal a morphological transition of FZNCs from smooth spherical nanoparticles to rough particles adorned with surface spikes, which remain stable upon prolonged exposure at this pH (Fig. S9). The corresponding

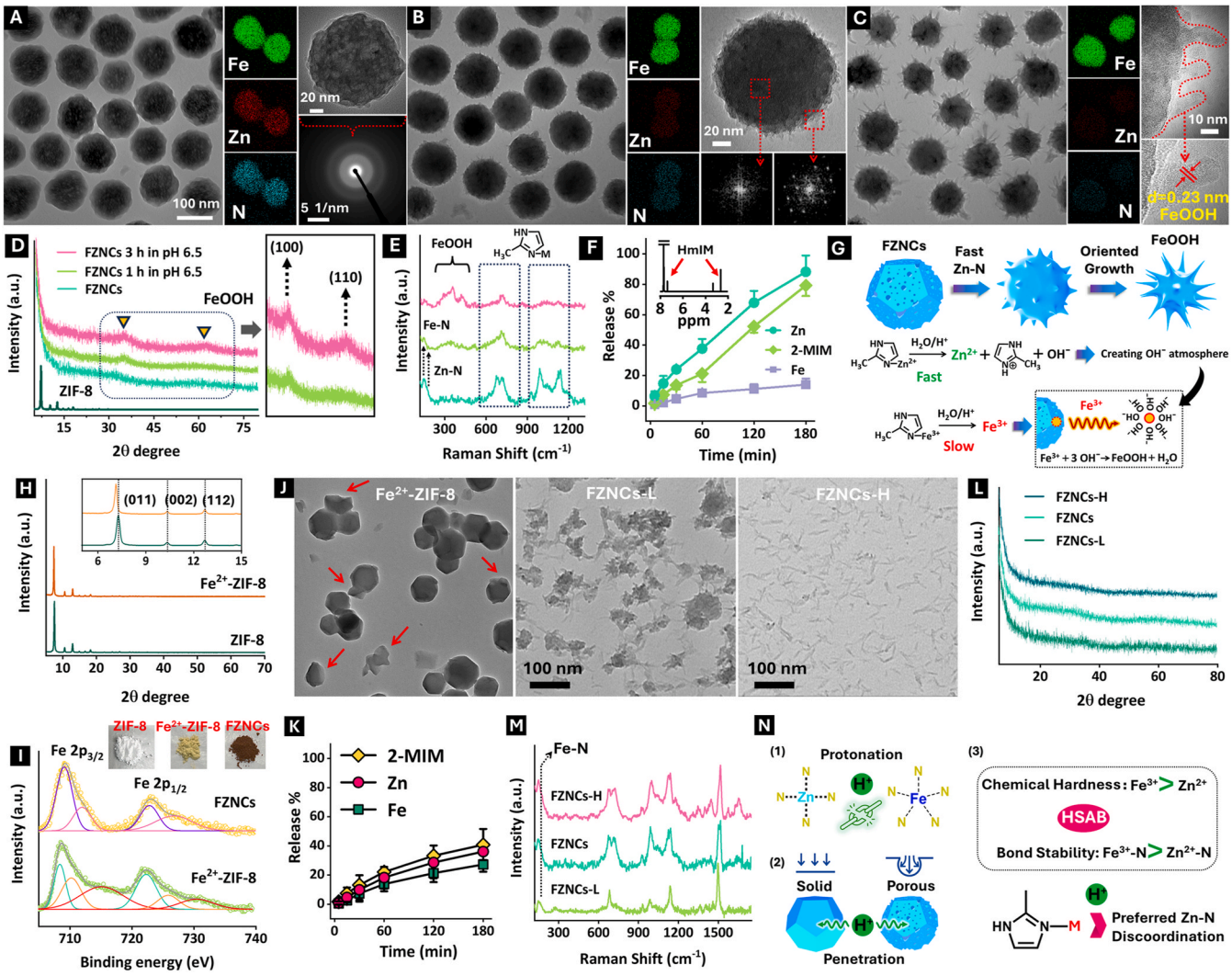


**Fig. 2. Acid-triggered structural and compositional transformation of FZNCs.** TEM, elemental mapping, selected area electron diffraction (SAED), and high-resolution TEM (HRTEM) images of FZNCs after incubation at pH 6.5 for (A) 0 h, (B) 1 h, and (C) 3 h, illustrating the acid-triggered morphological evolution from smooth spherical particles to spiky FeOOH nanostructures. (D) XRD patterns (inset: enlarged view of FeOOH diffraction peaks) and (E) Raman spectra of FZNCs after 0, 1, and 3 h of pH 6.5 treatment. (F) Release profiles of Zn, Fe, and HmIM at pH 6.5. The inset shows the NMR spectra for HmIM quantification. (G) Schematic illustration of the transformation mechanism. (H) XRD patterns (inset: enlarged low-angle region showing (011), (002), and (112) reflections) and (I) XPS spectra of ZIF-8, $Fe^{2+}$-ZIF-8, and FZNCs. (J) TEM images of $Fe^{2+}$-doped ZIF-8, FZNCs-L and FZNCs-H nanoparticles after acid treatment (pH 6.5 for 3 h). (K) The time-dependent release profiles of $Fe^{2+}$-doped ZIF-8 nanoparticles under pH 6.5 treatment. (L) XRD patterns and (M) Raman spectra of FZNCs, FZNCs-L and FZNCs-H. (N) Illustration of the structural features enabling the transformation of FZNCs into FeOOH under acidic conditions.

elemental mapping indicates a gradual reduction of Zn and N in the nanoparticles during the acidic treatment. At the same time, the selected area electron diffraction patterns transformed from an amorphous state, characterized by a halo ring pattern (Fig. 2A), to an amorphous core surrounded by a single crystalline shell showing clear diffraction spots (Fig. 2B). As shown in the HRTEM image (Fig. 2C), the outer crystalline spike exhibited a lattice fringe with a d spacing of 0.23 nm, that can be attributed to FeOOH. This observation aligns with previous reports that FeOOH typically grows into nanorods due to its intrinsic orientation growth [39,40] and is stable in mildly acidic conditions [41]. Furthermore, XRD patterns (Fig. 2D) of acid treated FZNCs exhibit two characteristic peaks assigned to (110) and (100) lattice plane of FeOOH, while Raman spectroscopy (Fig. 2E) reveals the decreased intensity of Fe–N and Zn–N signals as well as the appearance of FeOOH peaks. The release profiles of Zn, Fe, and HmIM (Fig. 2F and S10) reveal that Zn and HmIM rapidly released from FZNCs, while Fe released more gradually under pH 6.5 conditions. Based on above results, the acidity induced transformation of FZNCs is summarized in Fig. 2G. Initially, FZNCs maintained a smooth spherical morphology. Upon acid treatment, Zn–N bonds are cleaved more rapidly than Fe–N bonds, causing preferential Zn–N breakage and the release of HmIM linkers. The released HmIM are deprotonated by $H_2O$ to create an $OH^-$-rich microenvironment [42], thus the released $Fe^{3+}$ ions react with $OH^-$ to produce FeOOH, forming spikes *via* oriented growth on the outer surface of nanospheres.

Traditional divalent metal-doped ZIF-8 materials, such as those doped with $Cu^{2+}$, $Fe^{2+}$, and $Mn^{2+}$, retain the original crystalline structure of ZIF-8 and typically undergo simple degradation and metal ion release in acidic environments [43,44]. In contrast, FZNCs exhibit a unique response under acidic conditions, not only releasing $Zn^{2+}$ but also converting to FeOOH nanostructures. To elucidate the underlying mechanism behind this, we synthesized $Fe^{2+}$-doped ZIF-8 ($Fe^{2+}$-ZIF-8) as a control. The XRD patterns (Fig. 2H) and Fourier transform infrared spectroscopy (Fig. S11) of $Fe^{2+}$-ZIF-8 exhibit typical ZIF-8 structural characteristics. The intense diffraction peaks indicate a high crystallinity of $Fe^{2+}$-ZIF-8. X-ray photoelectron spectroscopy (XPS) (Fig. 2I) further confirms the different valence states of Fe in the samples, with $Fe^{2+}$

present in $Fe^{2+}$-ZIF-8 and $Fe^{3+}$ in FZNCs. The $Fe^{2+}$-ZIF-8 powder appears yellow and FZNCs appear red (inset of Fig. 2I), which is consistent with the typical colors of $Fe^{2+}$ and $Fe^{3+}$ compounds. Upon acid treatment, the TEM image of $Fe^{2+}$-ZIF-8 (Fig. S12) shows a degradation behaviour featured with debris from octahedral nanoparticles (Fig. 2J), similar to pure ZIF-8, without forming the characteristic spikes observed in FZNCs. The release profiles of Zn, Fe, and HmIM from $Fe^{2+}$-ZIF-8 (Fig. 2K) show that these components are released at similar rates, contrasting with the unique release dynamics observed in FZNCs.

In addition, the influence of $Fe^{3+}$ content on FZNCs-to-FeOOH transformation was also investigated. We fabricated FZNCs with the $Fe^{3+}$ content of 0.41 or 1.76 (Fe/Zn) termed as FZNCs-L or FZNCs-H (as determined by ICP-OES in Table S1), separately. The XRD patterns (Fig. 2L) and Raman spectra (Fig. 2M) indicate the successful fabrication of FZNCs with low and high $Fe^{3+}$ content, respectively. The TEM images (Fig. S12) exhibit a similar nanosphere morphology to FZNCs. As shown in Fig. 2J, insufficient or excessive $Fe^{3+}$ content in FZNCs failed to form FeOOH structures after acid treatment.

The transformation of FZNCs under acidic conditions can be attributed to their unique structural features as illustrated in Fig. 2N. (1) Different from ZIF-8, the increased Zn–N coordination number weakens the bond strength of Zn–N bond in FZNCs because the charge is distributed over more bonds. This makes it easier to protonate HmIM and break Zn–N coordination in FZNCs under acid conditions in

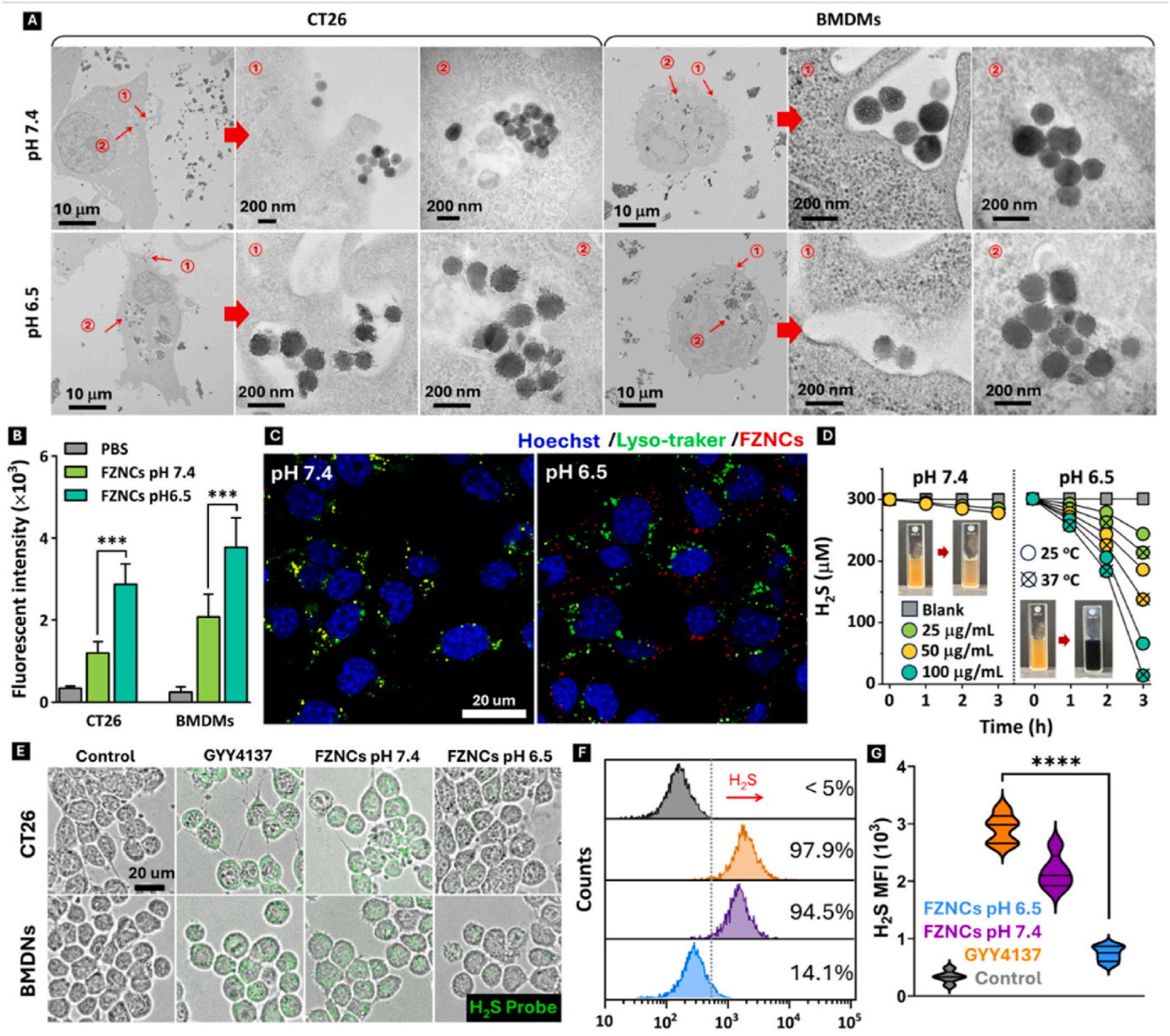


**Fig. 3. Acid-responsive cellular uptake and $H_2S$ depletion by FZNCs.** (A) Bio-TEM images of CT26 cells and bone marrow-derived macrophages (BMDMs) incubated with FZNCs at pH 7.4 and pH 6.5 for 3 h. Labels ① and ② indicate the regions of interest that are shown as magnified views on the right. (B) Flow cytometry analysis of FZNCs uptake in CT26 cells and BMDMs after 3 h of incubation at pH 7.4 and pH 6.5 (PBS as control). (C) CLSM images showing lysosome escape of FZNCs in CT26 cells after 6 h of incubation at pH 7.4 or pH 6.5; nuclei stained with Hoechst (blue), lysosomes with Lysotracker (green), and FZNCs with Cy5.5 (red). (D) $H_2S$ reactivity of FZNCs at different concentrations (25, 50, 100 μg/mL), pHs (pH 7.4 and pH 6.5) and temperatures (25 °C and 37 °C); $Na_2S$ was used as the $H_2S$ donor, inset shows corresponding color changes. (E) Bright-field and fluorescence images of CT26 cells and BMDMs treated with PBS (control), GYY4137 ($H_2S$ donor), or FZNCs at pH 7.4 and pH 6.5 for 3 h. The intracellular $H_2S$ was visualized using a fluorescent $H_2S$ probe (green). (F) Flow cytometry analysis and (G) its quantification result of intracellular $H_2S$ levels in CT26 cells after treatment with GYY4137, FZNCs at pH 7.4, or FZNCs at pH 6.5. (For interpretation of the references to color in this figure legend, the reader is referred to the Web version of this article.)

comparison to ZIF-8 structure [45]. (2) The larger pores on FZNCs surface, possibly due to the acidic responsive leaching profiles, enable $H^+$ to penetrate into the interior structure, not remaining only at the outermost layer of the particles, thereby accelerating the dissociation process. (3) The dissociation process preferentially happened in $Zn^{2+}$-N bonds rather than $Fe^{3+}$-N because of the higher chemical hardness of $Fe^{3+}$ than $Zn^{2+}$, guided by the HSAB principle. Taking together, these structural features of FZNCs are essential to the transformation of FZNCs to FeOOH.

FZNCs have been demonstrated to transform from smooth nanoparticles to spiky rough nanoparticles under acidic conditions. This transformation is significant because rough nanoparticles exhibit enhanced interaction with cells and faster internalization [46,47]. We first tested the colloidal stability of FZNCs in simulated serum. As shown in Fig. S13, FZNCs showed negligible size variation and ion leakage in 10 % FBS media (DMEM or RPMI 1640) at 37 °C for 60 h. With stability ensured, we next examined the cellular uptake of FZNCs under neutral (pH 7.4) and acidic (pH 6.5) conditions. Bio-TEM images (Fig. 3A) reveal the uptake of FZNCs by CT26 colon cancer cells and bone marrow-derived macrophages (BMDMs) after 3 h of incubation. At pH 7.4, the smooth FZNCs predominantly remained outside the cells, as indicated by arrows 1 and 2, which denote amplified positions. In contrast, at pH 6.5, a significant portion of the FZNCs, now rough with surface spikes, efficiently entered the cells. The quantification result (Fig. 3B) also shows a significantly higher uptake of FZNCs at pH 6.5 compared to pH 7.4 in both CT26 cells and BMDMs, as analyzed by flow cytometry.

According to a previous report, the spike structure on the surface of nanoparticles helps penetrate through the endosomal membrane, which facilitates appropriate endosomal escape [48]. To evaluate the endosomal escape capability of FZNCs, the lysosomes were stained using Lysotracker for confocal laser scanning microscopy (CLSM) imaging. As shown in Fig. 3C, the red signals from FZNCs colocalized well with green signals from lysosome in CT 26 cells cultured under pH 7.4. Whereas no obvious colocalization could be found under pH 6.5, demonstrating the efficient endosome escape of FZNCs in acidic conditions. We also examined confocal images at an earlier time point and observed a similar pattern that FZNCs did not colocalize with lysosomes (Fig. S14). This supports our hypothesis that the spiky morphology of FZNCs enables them to physically pierce the endosomal membrane, thereby preventing its acidification and maturation into lysosomes. In addition, an enhanced cell toxicity of FZNCs could be observed under pH 6.5 (Fig. S15), which might be primarily due to the improved cellular uptake.

Besides the enhanced uptake, the generated FeOOH as a widely reported $H_2S$ trap agent is anticipated to reduce the excessive $H_2S$ in tumor [49]. To demonstrate this, the reactivity of FZNCs with $H_2S$ was firstly evaluated in $Na_2S$ ($H_2S$ donor) solution with different pH (7.4 and 6.5) and temperatures. The time-dependent $H_2S$ concentration curves are shown in Fig. 3D, FZNCs exhibited weak reactivity with $H_2S$ at neutral pH 7.4. A significantly higher reactivity at pH 6.5 compared to pH 7.4 was observed across all tested FZNCs concentrations (25, 50, and 100 μg/mL). Notably, the $H_2S$ depletion efficiency was further improved at physiological temperature (37 °C). To further assess the cellular $H_2S$ depletion ability of FZNCs, CT26 colon cancer cells or BMDMs were treated with FZNCs under different pH conditions and then imaged using CLSM with an $H_2S$ probe. For comparison, GYY4137, an intracellular $H_2S$ donor, was used as positive control, which showed no significant cell toxicity (Fig. S16). As exhibited in Fig. 3E, minimal $H_2S$ (green signal) was observed in the control group, indicating baseline $H_2S$ levels, while the GYY4137 group showed a significant increase of $H_2S$, reflecting elevated $H_2S$ due to the donor. FZNCs at pH 7.4 exhibited moderate level of $H_2S$, but substantially reduced $H_2S$ at pH 6.5. The quantification of intracellular $H_2S$ levels by flow cytometry (Fig. 3F and G) further demonstrate the effectiveness of FZNCs in depleting cellular $H_2S$ within acidic environments.

The unique functions of $H_2S$ in manipulating metabolisms inspired us to investigate the impact of FZNCs on metabolic reprogramming of cancer cells and macrophages [50,51]. Therefore, the oxygen consumption rate (OCR) and extracellular acidification rate (ECAR) measurements were performed in CT26 colon cancer cells and BMDMs, as depicted in Fig. 4A. In CT26 cells, the introduction of the $H_2S$ donor led to a decrease in OCR and increase in ECAR, indicating an upregulation of glycolysis, consistent with $H_2S$'s role in enhancing tumor glycolytic activity. When FZNCs were introduced, $H_2S$'s effect was slightly weakened. However, FZNCs with acid treatment induced a significant metabolic shift, *i.e.*, ECAR decreased while OCR increased, reflecting a transition from a glycolytic phenotype to OXPHOS. This suggests that FZNCs effectively reprogram the metabolic profile of CT26 cells from glycolysis to OXPHOS preferably in the acidic environment.

For BMDMs, the $H_2S$ donor enhanced OCR, implying a preference for OXPHOS. Upon treatment with FZNCs, especially in acid treated FZNCs group, there was a notable decrease in OCR and an increase in ECAR. This indicates that FZNCs can rewire the metabolism of BMDMs, shifting them away from OXPHOS and towards glycolysis. Different from CT26 cancer cells, FZNCs alone also caused a moderate metabolism shift. This is due to Fe's role in regulating macrophage metabolism and a similar phenomenon has been observed in our previous research [10]. The measurement of $^{13}C$-glucose flux in metabolites provides further evidence supporting these metabolic shifts (Fig. 4B). In CT26 cells, $H_2S^+$/$FZNCs^+$/$acid^+$ group showed a marked reduction in glycolytic metabolites such as 3 PG, PRY and LAC, while an increase in TCA products such as FUM and MAL compared to $H_2S^+$, aligning with the observed shift to OXPHOS. In contrast, BMDMs after $H_2S^+$/$FZNCs^+$/$acid^+$ treatment exhibited an enrichment of glycolytic metabolites, consistent with their shift towards glycolysis. These metabolomic changes demonstrate the ability of FZNCs to reprogram cancer cells and macrophages in opposing directions—shifting cancer cells from glycolysis to OXPHOS and macrophages from OXPHOS to glycolysis.

To further explore the metabolic impact of FZNCs treatment, untargeted metabolomic profiling was conducted in both CT26 cancer cells and BMDMs. The heatmap in Fig. 4C shows the relative abundance of intracellular metabolites, where distinct patterns were observed between the control and FZNCs groups. Notably, in CT26 cells, metabolites associated with glycolysis such as 3-phosphoglycerate and lactate were significantly downregulated, while tricarboxylic acid (TCA) cycle intermediates like citrate and fumarate were elevated, consistent with a shift toward oxidative phosphorylation. In contrast, BMDMs displayed an opposite trend—glycolytic metabolites were elevated, while several TCA cycle intermediates were decreased—supporting a shift toward glycolysis. Principal component analysis (PCA) further confirmed the global metabolic reprogramming (Fig. 4D and F). In both CT26 and BMDMs, the FZNCs-treated samples clustered separately from the controls, indicating distinct metabolic states. Volcano plots (Fig. 4E and 4G) also identified >70 % significantly altered metabolites (fold change >1.5, $p < 0.05$). To gain pathway-level insights, enrichment analysis was performed (Fig. 4H) using the Reactome database [52]. In CT26 cells, the most activated pathways following FZNCs treatment included the TCA cycle, vitamin and cofactor metabolism, and fatty acid oxidation—consistent with enhanced mitochondrial function. Conversely, BMDMs exhibited upregulation of glycolysis and fatty acid synthesis, suggesting a metabolic shift away from mitochondrial respiration toward aerobic glycolysis.

Given that the metabolic function of FZNCs relies on tumor-specific $H_2S$ depletion, we specifically examined sulfur-related metabolic pathways (Fig. 4I). In CT26 cells, the sulfur amino acid metabolism pathway—closely associated with endogenous $H_2S$ production—was markedly downregulated after FZNCs treatment. Additionally, pathways related to mitochondrial iron-sulfur cluster biogenesis and purine metabolism also showed suppression. In BMDMs, FZNCs treatment led to the upregulation of redox-related pathways such as reactive oxygen/

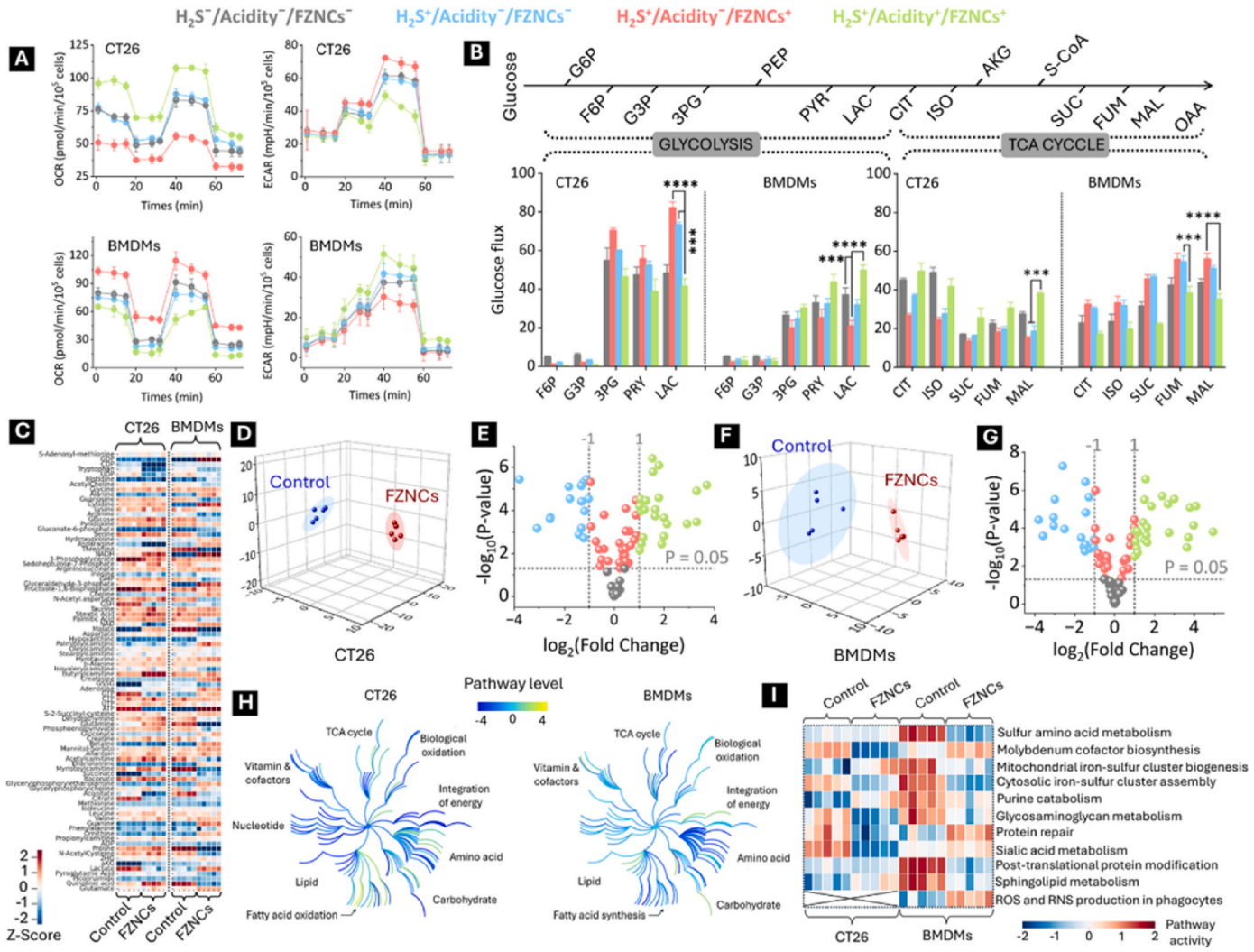


**Fig. 4. Metabolic reprogramming of CT26 cells and BMDMs mediated by FZNCs.** (A) Oxygen consumption rate (OCR) and extracellular acidification rate (ECAR) profiles in CT26 cancer cells and BMDMs following treatment with or without FZNCs and/or acidic conditions ($H^+$). (B) Metabolic flux analysis using $^{13}$C-glucose tracing in CT26 cells and BMDMs. Full names of metabolites are listed in Table S4. (C) Untargeted metabolite expression profiles in CT26 cells and BMDMs treated with control ($H_2S$ only) or acid-activated FZNCs ($H_2S/H^+$/FZNCs). (D–G) Principal component analysis (PCA, D, F) and volcano plots (E, G) of metabolic shifts in CT26 cells and BMDMs upon FZNCs treatment. (H) Metabolic pathway-level enrichment analysis annotated in the Reactome database. (I) Pathway activity heatmap of sulfur-related metabolic pathways in CT26 cells and BMDMs.

nitrogen species (ROS/RNS) production and post-translational modification. These pathway-specific responses provide strong evidence that FZNC-mediated $H_2S$ depletion alters intracellular sulfur metabolism and drives distinct metabolic reprogramming in cancer cells and macrophages.

To characterize the immunogenicity resulting from FZNCs-mediated metabolic reprogramming, we measured key immunoregulating metabolites secreted by CT26 cells under different conditions. As shown in Fig. 5A, cells treated with GYY4137 elevated the secretion of lactate, kynurenine, and adenosine, known metabolites associated with immunosuppressive functions in the tumor microenvironment, but reduced immunostimulatory ATP production. In contrast, FZNCs treatment, especially under acidic conditions (FZNCs/$H^+$), substantially reduced the immunosuppressive metabolites while boosting ATP secretion. Immunofluorescence imaging demonstrated significantly increased surface expression of calreticulin (CRT), a hallmark of enhanced immunogenicity, in FZNCs/$H^+$ treated cancer cells (Fig. 5B). According to previous reports, these immunogenic molecular patterns can actively recruit dendritic cells for immune activation [53]. Thus, we next performed the dendritic cell (DC) maturation assay *via* a coculture method (Fig. 5C). CT26 cancer cells pretreated with FZNCs/$H^+$ promoted the highest DC maturation rate compared to control or GYY4137-treated cells (Fig. 5D and S17). Correlation analysis indicated strong negative relationships between immunosuppressive metabolite levels (adenosine, kynurenine, lactate) and DC maturation efficiency (Fig. 5E), as well as a positive ATP-DC maturation relationship, supporting the direct link between metabolic modulation and enhanced cancer cell immunogenicity.

We next studied the influence of FZNCs-mediated metabolic reprogramming on the immunogenicity of macrophages, where cell phenotype and cytokines secretion were tested. Firstly, the macrophage polarization was investigated by flow cytometry analysis (Fig. 5F and G). Treatment with the $H_2S$ donor strongly induced the immunosuppressive M2 phenotype (CD206-positive cells, 94.5 %), which is consistent with previous reports [54]. Whereas FZNCs treatment reversed this trend, notably reducing CD206-positive cells to 29.2 % under acidic conditions. Concurrently, FZNCs/$H^+$ treatment significantly elevated the expression of the M1-associated markers CD80 and IL-12, indicating a clear shift towards an immunostimulatory M1 phenotype. A moderate M1 polarization was also found in the FZNCs

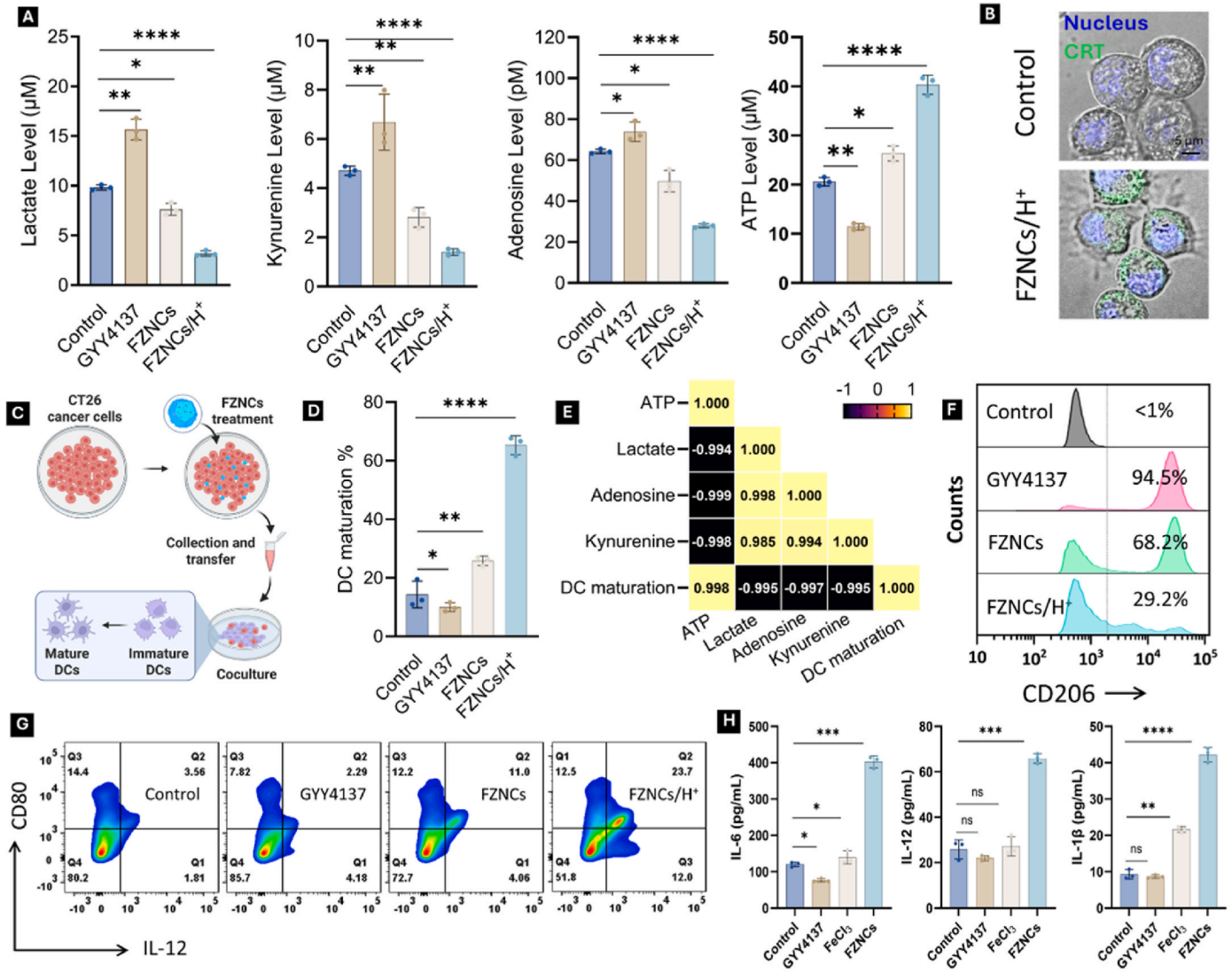


**Fig. 5. Enhanced immunogenicity *via* metabolic reprogramming by FZNCs**. (A) Quantification of extracellular immunoregulating metabolites (lactate, ATP, kynurenine, adenosine) in the supernatants of CT26 cancer cells treated under different conditions. (B) Immunofluorescence imaging of calreticulin (CRT) exposure in CT26 cells following FZNCs treatment. GYY4137 was used as intracellular $H_2S$ donor. (C) Schematic illustration of dendritic cell (DC) maturation assay co-cultured with pretreated CT26 cancer cells and (D) the quantification analysis by flow cytometry. (E) Correlation heatmap between DC maturation and metabolite levels. (F–G) Flow cytometry analysis of macrophage polarization after various treatments. CD206 was used as M2 phenotype marker and CD80/IL-12 was used as M1 phenotype marker. (H) ELISA analysis of cytokines IL-6, IL-12, and TNF-α secreted by macrophages treated as indicated. Data presented as mean ± SD; *p < 0.05, **p < 0.01, ***p < 0.001, ****p < 0.0001.

group under neutral conditions, indicating a contribution by the typical $Fe^{3+}$-based M1 polarization pathway. Consistent with these findings, ELISA assays demonstrated a robust increase in pro-inflammatory cytokines IL-6, IL-12, and TNF-α from macrophages treated with acid-activated FZNCs (Fig. 5H). However, we observed that treatment with $Fe^{3+}$ or FZNCs alone under neutral conditions resulted in only modest increases in pro-inflammatory cytokine secretion. This indicates the pronounced enhancement of macrophage immunogenicity by acid-activated FZNCs is primarily attributable to the reprograms cellular metabolism rather than the widely reported $Fe^{2+/3+}$-driven polarization pathways. Collectively, these results strongly support the capacity of acid-activated FZNCs to enhance tumor immunogenicity by simultaneously reducing tumor-derived immunosuppressive metabolites and reprogramming macrophages toward a pro-inflammatory phenotype.

To test whether our FZNCs could synchronously regulate metabolism in both cancer cells and macrophages *in vivo*, we built a mouse model bearing CT26 tumors (Fig. 6A). After intravenous administration of FZNCs, CT26 cancer cells and tumor-associated macrophages (TAMs) were rapidly isolated from tumor tissues using an optimized low-temperature magnetic sorting protocol, utilizing EpCAM and F4/80 antibodies for positive selection. Notably, CT26 cells exhibit robust EpCAM expression (>99 %, Fig. S18), ensuring efficient cell enrichment for metabolic analysis. Single-cell metabolomic analysis *in vivo* is technically challenging, as tissue processing and cell sorting procedures inherently influence the highly dynamic nature of the metabolome. To validate our experimental design, we first simulated the digestion and sorting workflow using cultured CT26 cells an BMDMs *in vitro*. Metabolite profiles before and after simulated procedures revealed that over 70 % of analyzed metabolites displayed acceptable variations (<20 %, Fig. 6B and C and S19). However, certain metabolites, such as ATP and NADPH, exhibited notable variability (up to ~50 %), highlighting the importance of selecting stable metabolites for *in vivo* analysis. Therefore, we identified and selected 50 metabolites with minimal processing-induced variability for subsequent *in vivo* profiling. As shown in Fig. S20, the *in vivo* metabolic analysis clearly demonstrated that FZNCs induced robust, simultaneous, and opposite metabolic reprogramming

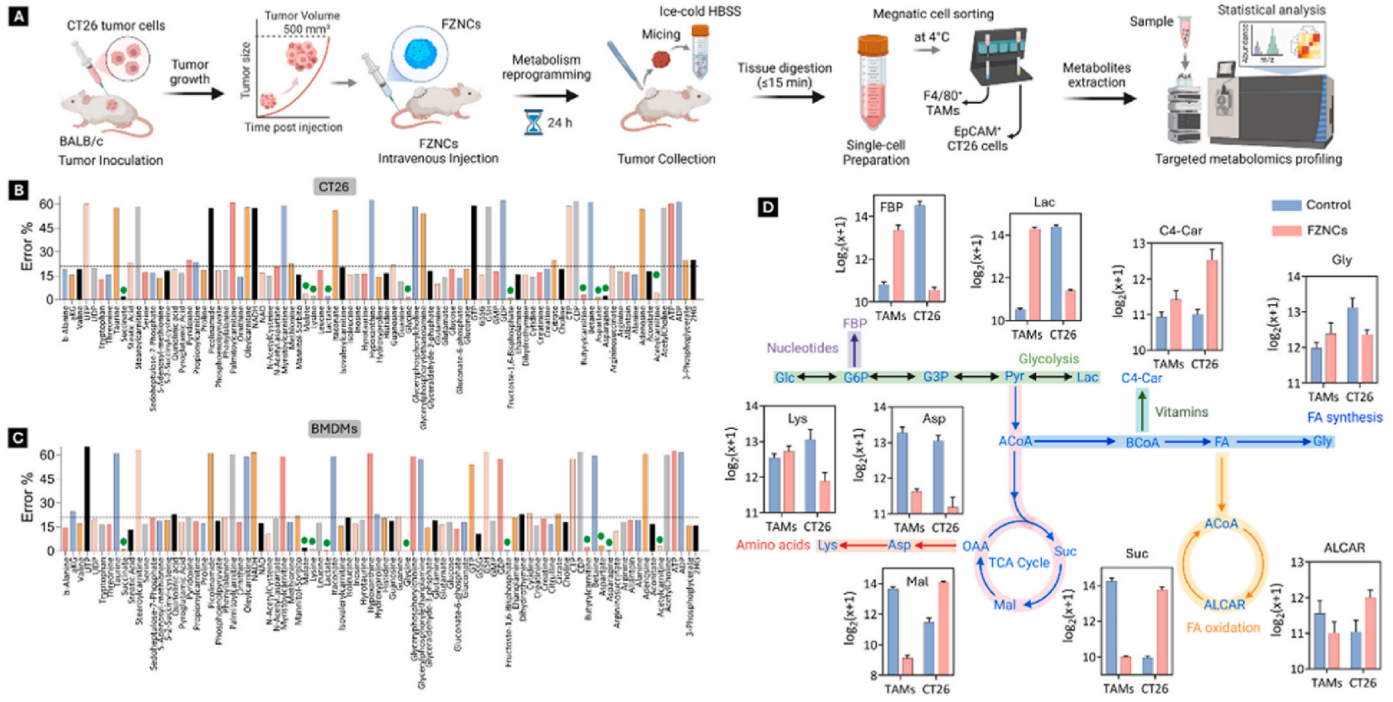


**Fig. 6.** ***In vivo*** **metabolic reprogramming of CT26 cancer cells and TAMs mediated by FZNCs.** (A) Experimental workflow for *in vivo* untargeted metabolomics analysis of tumor tissue-resident CT26 cancer cells and TAMs following magnetic sorting. Evaluation of metabolic alterations induced by digestion and magnetic sorting procedures in cultured (B) CT26 cells and (C) BMDMs. Bars indicate relative error percentages of metabolite levels pre- and post-processing. The dashed line represents an error margin of 20 %. Green dots represent selected metabolites with minimal procedural variations. (D) Representative metabolic pathway diagram and relative abundance profiles of selected metabolites in sorted CT26 cancer cells and TAMs from tumor tissues of mice treated with FZNCs. Data represents mean ± SD (5 mice was used in each group). (For interpretation of the references to color in this figure legend, the reader is referred to the Web version of this article.)

in CT26 cancer cells and TAMs. To further exclude the procedural variations, we selected the most stable 9 metabolites (marked by green dots in Fig. 6B and C) and illustrated their abundance in a metabolic pathway diagram. As displayed in Fig. 6D, in CT26 cells from FZNC-treated tumors, glycolysis-related metabolite (Lac) was notably decreased, while metabolites associated with the tricarboxylic acid (TCA) cycle (Suc and Mal) and fatty acid oxidation (ALCAR) significantly increased. In contrast, TAMs isolated from the same tumors displayed upregulated glycolysis and fatty acid synthesis (Gly) metabolites and decreased levels of TCA cycle intermediates, suggesting a metabolic shift from oxidative phosphorylation toward glycolysis.

These *in vivo* results highlight the dual functionality of FZNCs in precisely orchestrating metabolic shifts tailored to distinct cell types within the same tumor microenvironment. While minor technical variations inherent to sample preparation and cell sorting procedures are unavoidable, the observed synchronous yet opposing metabolic reprogramming represents a significant advance, providing, to the best of our knowledge, the first demonstration of nanomaterial-induced simultaneous and opposite *in vivo* metabolic regulation of cancer cells and macrophages.

Encouraged by our *in vivo* metabolic regulation results, we next evaluated the performance of FZNCs in reversing immunosuppressive tumor microenvironment for cancer immunotherapy. One important feature of tumor tissue is the acidic microenvironment, which has been widely exploited to develop acid responsive delivery strategies for therapeutic agents [55]. The acidic nature of the tumor microenvironment is expected to trigger the transformation of FZNCs from smooth to rough nanoparticles, enhancing their cellular uptake and accumulation in tumor tissues. This inspired us to explore the biodistribution of FZNCs in the tumor model. To directly visualize the *in vivo* biodistribution, FZNCs were labelled with fluorescent Cy-5.5 and intravenously injected into tumor-bearing mice. The distribution at various time points post-injection (3, 6, 9, 12, 24, and 48 h) was imaged by IVIS (Fig. 7A). $Fe^{2+}$-ZIF-8 nanoparticles were also set here as comparison. The imaging results show that FZNCs exhibit prolonged retention at the tumor site compared to $Fe^{2+}$-ZIF-8, indicating their good tumor-targeting capability. Besides roughness, presumably the good colloidal stability and acid responsive change in surface (Fig. S21) also contribute to its good *in vivo* tumor targeting ability. Moreover, PEGylation of FZNCs exhibited a further improvement in tumor accumulation (Fig. S22), implying that FZNCs are feasible for surface modifications and the enabled new biofunctions. The biodistribution of FZNCs in major organs and tumors was assessed by quantifying Zn and Fe content *via* ICP-MS. As shown in Fig. 7B, a significant amount of Fe accumulated in the tumor tissue, whereas Zn levels were minimal. This discrepancy likely results from the acid-responsive disassembly of FZNCs in the extracellular tumor microenvironment, where $Zn^{2+}$ ions are rapidly released and cleared due to the high interstitial fluid pressure and dynamic ion exchange. In contrast, $Fe^{3+}$ within the FZNCs is converted into rough-surfaced FeOOH nanoparticles, which exhibit enhanced cellular uptake and are more readily retained within the tumor, leading to selective Fe enrichment.

The $H_2S$ depletion capability of FZNCs was further evaluated *in vivo*. For comparison, the I194496, an inhibitor targeting cystathionine γ-lyase and endogenous $H_2S$ production [56], was also used. As shown in Fig. 7C and D, while I194496 effectively reduced $H_2S$ levels, this reduction occurred non-specifically in both the liver and tumor tissue, raising concerns about potential systemic toxicity. In contrast, FZNCs selectively reduced $H_2S$ levels within the tumor with minimal impact on non-target organs such as the liver, indicating their specificity for tumor-associated $H_2S$ depletion.

To evaluate the immunotherapeutic performance of FZNCs, CT26 colon tumor-bearing mice were treated with FZNCs, PDL1 immune checkpoint inhibitors (anti-PDL1) or their combination and then the tissues and blood were harvested for further analysis, as outlined in the experimental setup (Fig. 7E). The tumor growth profile in Fig. 7G

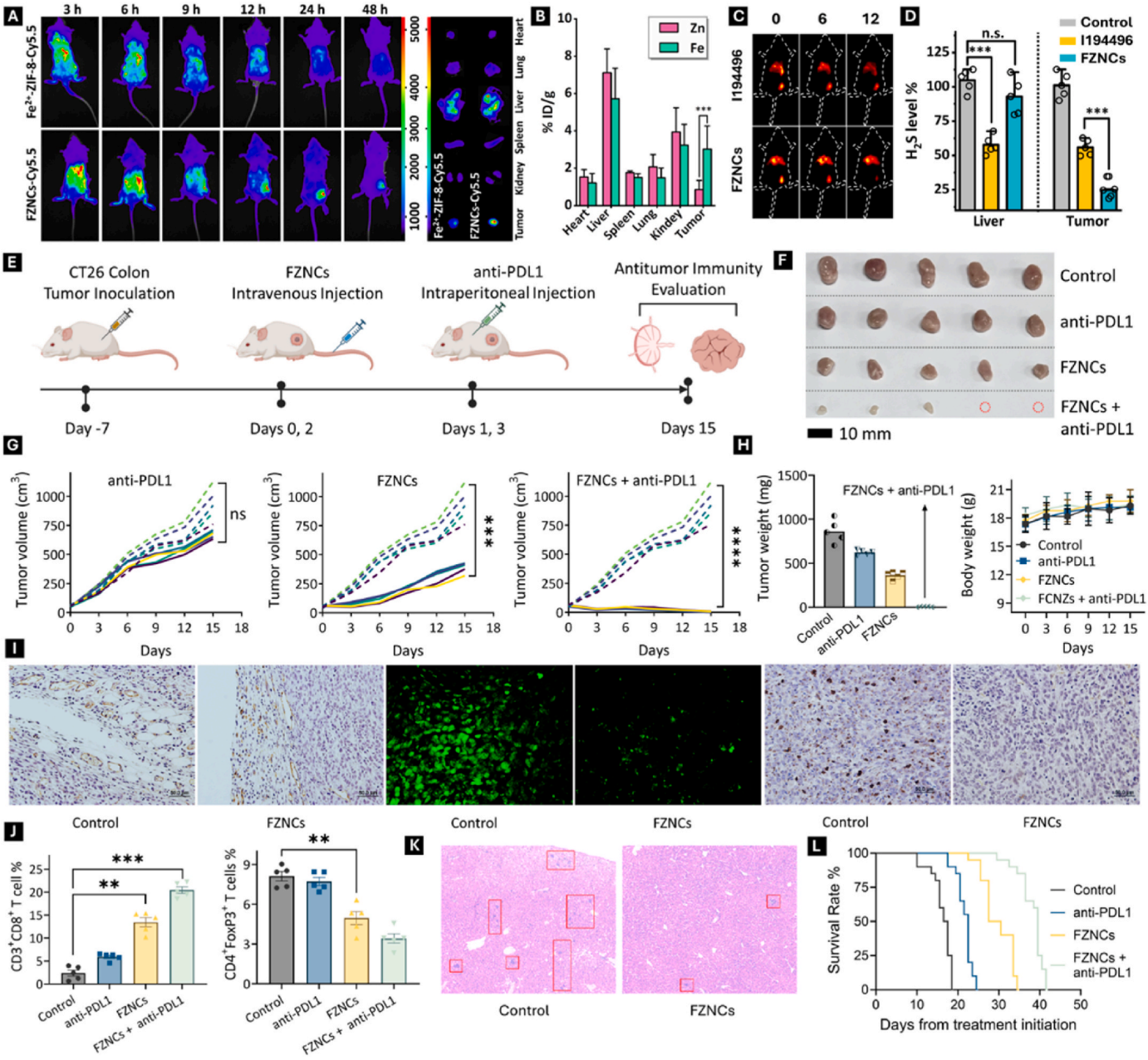


**Fig. 7.** ***In vivo*** **evaluation of antitumor efficacy and immune activation by FZNCs and combination therapy with anti-PDL1.** (A) IVIS imaging of FZNCs-Cy5.5 and $Fe^{2+}$-ZIF-8-Cy5.5 in tumor-bearing mice at various time points post-injection. (B) ICP quantification analysis of Zn and Fe elements in different organs and tumors. (C) *In vivo* imaging of $H_2S$ in CT26 tumor bearing mice after treatment with FZNCs or I194496 at different time intervals. I194496 is a small-molecule inhibitor that suppresses endogenous $H_2S$ generation. (D) Quantification of $H_2S$ in the liver and tumor tissues. (E) Experimental design for the CT26 tumor-bearing mouse model. (F) Representative tumor images from each treatment group. (G) Tumor growth curves monitored over 18 days. (H) Tumor weights at the end of treatment and body weight tracking throughout the treatment duration. (I) Immunohistochemical staining of CD31 (vascular marker), IDO (immune suppressive marker), and immunofluorescent staining of Ki-67 (proliferation marker) in tumor tissues. (J) Flow cytometric quantification of tumor-infiltrating cytotoxic ($CD3^+CD8^+$) T cells and immunosuppressive regulatory ($CD4^+Foxp3^+$) T cells. (K) H&E staining of lung tissues showing metastatic tumor nodules (circled). (L) Survival analysis of mice treated with FZNCs alone or in combination with anti-PDL1 therapy. 5 mice per group were used in experiments A–K, and 20 mice per group for survival analysis.

revealed significant tumor inhibition by FZNCs, with the greatest effect observed in the combination therapy group (FZNCs + anti-PDL1). Representative tumor images and tumor weight data (Fig. 7F–H) further corroborated these findings, demonstrating the potent therapeutic effects of FZNCs and their synergistic interaction with anti-PDL1 blockade. Notably, previous studies have reported that zinc ions can activate antitumor immunity by enhancing antigen presentation, modulating tumor-associated macrophage polarization, and promoting T cell-mediated immune responses [57]. In our study, the contribution of $Zn^{2+}$ to the therapeutic effect appears to be limited due to its low accumulation within the tumor microenvironment (Fig. 7B). Importantly, body weight remained stable across all treatment groups (Fig. 7H), and H&E staining of major organs, including the heart, liver, spleen, lung, and kidney, showed no signs of tissue damage (Fig. S23), further indicating the low systemic toxicity of FZNCs.

To understand the underlying mechanisms of tumor suppression, tumor tissues were analyzed for key biomarkers associated with tumor progression and immune modulation. The CD31 staining revealed a

decrease angiogenesis in the FZNC-treated group, while Ki-67 staining revealed a significant reduction in tumor cell proliferation (Fig. 7I and S24-25). According to previous reports, this can be attributed to the synchronous metabolic reprogramming of both cancer cells and macrophages that reduces the secretion of pro-angiogenic factors such as VEGF and IL-10 [58,59]. Furthermore, immunohistochemical staining revealed a marked reduction in IDO (indoleamine 2,3-dioxygenase) expression in the FZNC-treated groups, which is known to inhibit T-cell activity (Fig. 7I and S24-25). To demonstrate this, tumor-infiltrating lymphocytes were further analyzed by flow cytometry. As shown in Fig. 7J–S26 and S27, FZNCs treatment significantly increased the proportion of cytotoxic $CD3^+CD8^+$ T cells, while reducing the population of immunosuppressive $CD4^+Foxp3^+$ regulatory T cells. These changes indicate that FZNCs not only promote immune cell infiltration into the tumor microenvironment but also shift the immune balance toward a more active antitumor state. To further assess the *in vivo* immune-regulatory effect of FZNCs, we treated the tumor with FZNCs alone and then analyzed $CD8^+IFN\gamma^+$ T cells and inflammatory cytokines after 96 h. As shown in Fig. S28, FZNCs treatment elevated $CD8^+IFN\gamma^+$ T cells population around 10 times to control group, together with increased levels of TNF-α and IL-12p40, suggesting FZNCs triggered a pro-inflammatory tumour microenvironment.

To evaluate the potential of FZNCs in preventing tumor metastasis, lung tissues were examined for metastatic nodules *via* H&E staining (Fig. 7K). Mice treated with FZNCs displayed significantly fewer tumor nodules in the lungs compared to controls, indicating that FZNCs can effectively inhibit metastatic spread, a critical feature for improving long-term outcomes in cancer therapy. Finally, the survival benefits of FZNCs were assessed through a Kaplan-Meier survival analysis (Fig. 7L). FZNC treatment significantly extended the survival of tumor-bearing mice compared to controls, with the combination therapy group achieving the longest survival. This highlights the potential of FZNCs to enhance the efficacy of existing immunotherapies, particularly immune checkpoint inhibitors.

## 3. Conclusion

This study demonstrates the potential of Fe–Zn bimetallic nanocomplexes (FZNCs) as a tumor-activatable platform for cancer immunotherapy. Unlike conventional divalent Fe-doped ZIF-8, our trivalent Fe-doped framework disrupts the classical ZIF-8 structure, enabling a unique transformation into spiky FeOOH nanoparticles under acidic tumor conditions. This structural transformation enhances cellular uptake, selectively reduces tumor-associated $H_2S$, and reprograms metabolic pathways in both cancer cells and macrophages. The resulting metabolic rewiring boosts tumor immunogenicity by promoting dendritic cell maturation, macrophage polarization toward an M1 phenotype, and T-cell infiltration, thereby enhancing antitumor immune responses. *In vivo*, FZNCs effectively suppressed tumor growth, reduced metastasis, and extended survival, with the combination of FZNCs and anti-PDL1 achieving synergistic therapeutic effects. Importantly, FZNCs exhibited negligible systemic toxicity, demonstrating their translation potential. These findings highlight FZNCs as a novel material-driven strategy for synchronizing metabolic and immunological reprogramming, paving the way for next-generation cancer immunotherapies.

## CRediT authorship contribution statement

**Zan Dai:** Writing – review & editing, Writing – original draft, Visualization, Validation, Supervision, Project administration, Methodology, Investigation, Formal analysis, Conceptualization. **Qiaoyun Wang:** Visualization, Validation, Software, Resources, Project administration, Methodology, Investigation, Formal analysis, Data curation. **Ming Zhang:** Software, Methodology. **Yiru Shi:** Methodology, Investigation. **Yannan Yang:** Writing – review & editing, Resources. **Hao Song:** Resources. **Runming Wang:** Software, Methodology. **Bernt Johannessen:** Methodology, Investigation. **Xu Zhen:** Writing – review & editing, Visualization. **Chengzhong Yu:** Writing – review & editing, Supervision, Resources, Project administration, Funding acquisition.

## Declaration of competing interest

The authors declare that they have no known competing financial interests or personal relationships that could have appeared to influence the work reported in this paper.

## Acknowledgements

The authors acknowledge the financial support from the Australian Research Council (DP210102277), the Queensland Government and Science and Technology Commission of Shanghai Municipality, China (No. 19JC1412100), and the National Natural Science Foundation of China (No. 52173130). We also thank the technical assistance from the Australian National Fabrication Facility, the Australian Microscopy and Microanalysis Research Facility at the Centre for Microscopy and Microanalysis, Q-MAP Metabolomics and Proteomics, Australian Synchrotron, The University of Queensland's Biological Resources, and QIMR Berghofer Medical Research Institute.

## Appendix A. Supplementary data

Supplementary data to this article can be found online at https://doi.org/10.1016/j.biomaterials.2025.123655.

## Data availability

Data will be made available on request.

## References

[1] I. Martínez-Reyes, N.S. Chandel, Cancer metabolism: looking forward, Nat. Rev. Cancer 21 (2021) 669.
[2] A. Schulze, A.L. Harris, How cancer metabolism is tuned for proliferation and vulnerable to disruption, Nature 491 (2012) 364.
[3] U. Basak, T. Sarkar, S. Mukherjee, S. Chakraborty, A. Dutta, S. Dutta, D. Nayak, S. Kaushik, T. Das, G. Sa, Tumor-associated macrophages: an effective player of the tumor microenvironment, Front. Immunol. 14 (2023) 1295257.
[4] I. Larionova, G. Tuguzbaeva, A. Ponomaryova, M. Stakheyeva, N. Cherdyntseva, V. Pavlov, E. Choinzonov, J. Kzhyshkowska, Tumor-associated macrophages in human breast, colorectal, lung, ovarian and prostate cancers, Front. Oncol. 10 (2020) 566511.
[5] M. De Martino, J.C. Rathmell, L. Galluzzi, C. Vanpouille-Box, Cancer cell metabolism and antitumour immunity, Nat. Rev. Immunol. 24 (2024) 654.
[6] M. Wenes, M. Shang, M. Di Matteo, J. Goveia, R. Martín-Pérez, J. Serneels, H. Prenen, B. Ghesquière, P. Carmeliet, M. Mazzone, Macrophage metabolism controls tumor blood vessel morphogenesis and metastasis, Cell Metab. 24 (2016) 701.
[7] R.B. Hamanaka, N.S. Chandel, Warburg effect and redox balance, Science 334 (2011) 1219.
[8] M. Li, Y. Yang, L. Xiong, P. Jiang, J. Wang, C. Li, Metabolism, metabolites, and macrophages in cancer, J. Hematol. Oncol. 16 (2023) 80.
[9] Z. Dai, Q. Wang, J. Tang, R. Qu, M. Wu, H. Li, Y. Yang, X. Zhen, C. Yu, A Sub-6 nm $MnFe_2O_4$-dichloroacetic acid nanocomposite modulates tumor metabolism and catabolism for reversing tumor immunosuppressive microenvironment and boosting immunotherapy, Biomaterials 284 (2022) 121533.
[10] Z. Gu, T. Liu, C. Liu, Y. Yang, J. Tang, H. Song, Y. Wang, Y. Yang, C. Yu, Ferroptosis-strengthened metabolic and inflammatory regulation of tumor-associated macrophages provokes potent tumoricidal activities, Nano Lett. 21 (2021) 6471.
[11] X. Liang, X. Chen, Y. Yan, A. Cheng, J. Lin, Y. Jiang, H. Chen, J. Jin, X. Luan, Targeting metabolism to enhance immunotherapy within tumor microenvironment, Acta Pharmacol. Sin. 45 (2024) 2011.
[12] M. Cerezo, S. Rocchi, Cancer cell metabolic reprogramming: a keystone for the response to immunotherapy, Cell Death Dis. 11 (2020) 964.
[13] C. Dussold, K. Zilinger, J. Turunen, A.B. Heimberger, J. Miska, Modulation of macrophage metabolism as an emerging immunotherapy strategy for cancer, J. Clin. Investig. 134 (2024) 175445.
[14] P. Saha, P. Ettel, T. Weichhart, Leveraging macrophage metabolism for anticancer therapy: opportunities and pitfalls, Trends Pharmacol. Sci. 45 (2024) 335.
[15] S. Gheibi, A.P. Samsonov, S. Gheibi, A.B. Vazquez, K. Kashfi, Regulation of carbohydrate metabolism by nitric oxide and hydrogen sulfide: implications in diabetes, Biochem. Pharmacol. 176 (2020) 113819.

[16] R.H. Wang, P.R. Chen, Y.T. Chen, Y.C. Chen, Y.H. Chu, C.C. Chien, P.C. Chien, S. Y. Lo, Z.L. Wang, M.C. Tsou, S.Y. Chen, G.S. Chiu, W.L. Chen, Y.H. Wu, L.H. C. Wang, W.C. Wang, S.Y. Lin, H.J. Kung, L.H. Wang, H.C. Cheng, K.T. Lin, Hydrogen sulfide coordinates glucose metabolism switch through destabilizing tetrameric pyruvate kinase M2, Nat. Commun. 15 (2024) 7463.
[17] N. Zhao, G. Wu, L. Zhao, $H_2S$ as a metabolic saboteur, Nat. Metab. 6 (2024) 1431.
[18] M. Libiad, V. Vitvitsky, T. Bostelaar, D.W. Bak, H.-J. Lee, N. Sakamoto, E. Fearon, C.A. Lyssiotis, E. Weerapana, R. Banerjee, Hydrogen sulfide perturbs mitochondrial bioenergetics and triggers metabolic reprogramming in colon cells, J. Biol. Chem. 294 (2019) 12077.
[19] C. Szabo, C. Coletta, C. Chao, K. Módis, B. Szczesny, A. Papapetropoulos, M. R. Hellmich, Tumor-derived hydrogen sulfide, produced by cystathionine-β-synthase, stimulates bioenergetics, cell proliferation, and angiogenesis in colon cancer, Proc. Natl. Acad. Sci. 110 (2013) 12474.
[20] J. Machado Neto, A. Cerqueira, S. Veríssimo Filho, M. Muscará, S. Costa, L. Lopes, Hydrogen sulfide signaling in the tumor microenvironment: implications in cancer progression and therapy, Antioxidants Redox Signal. 40 (2023) 250.
[21] M.A. Rahman, B.M. Cumming, K.W. Addicott, H.T. Pacl, S.L. Russell, K. Nargan, T. Naidoo, P.K. Ramdial, J.H. Adamson, R. Wang, Hydrogen sulfide dysregulates the immune response by suppressing central carbon metabolism to promote tuberculosis, Proc. Natl. Acad. Sci. 117 (2020) 6663.
[22] G.V. Velmurugan, H. Huang, H. Sun, J. Candela, M.K. Jaiswal, K.D. Beaman, M. Yamashita, M. Prakriya, C. White, Depletion of $H_2S$ during obesity enhances store-operated $Ca^{2+}$ entry in adipose tissue macrophages to increase cytokine production, Sci. Signal. 8 (2015) 128.
[23] S. Houston, Tissue differences in macrophage metabolism, Nat. Immunol. 24 (2023) 378.
[24] W. Gao, Y.F. Liu, Y.X. Zhang, Y. Wang, Y.Q. Jin, H. Yuan, X.Y. Liang, X.Y. Ji, Q. Y. Jiang, D.D. Wu, The potential role of hydrogen sulfide in cancer cell apoptosis, Cell Death Discov. 10 (2024) 114.
[25] C. Szabo, Gasotransmitters in cancer: from pathophysiology to experimental therapy, Nat. Rev. Drug Discov. 15 (2016) 185.
[26] A.K. Mustafa, M.M. Gadalla, N. Sen, S. Kim, W. Mu, S.K. Gazi, R.K. Barrow, G. Yang, R. Wang, S.H. Snyder, $H_2S$ signals through protein S-sulfhydration, Sci. Signal. 2 (2009) 72.
[27] T. Nguyen, P. Nguyen, S.H. Park, C.H. Jung, T.I. Jeon, Hydrogen sulfide and liver health: insights into liver diseases, Antioxidants Redox Signal. 40 (2023) 122.
[28] K. Wang, S. Ahmad, M. Cai, J. Rennie, T. Fujisawa, F. Crispi, J. Baily, M.R. Miller, M. Cudmore, P.W.F. Hadoke, R. Wang, E. Gratacós, I.A. Buhimschi, C.S. Buhimschi, A. Ahmed, Dysregulation of hydrogen sulfide producing enzyme cystathionine γ-lyase contributes to maternal hypertension and placental abnormalities in preeclampsia, Circulation 127 (2013) 2514.
[29] M.R. Hellmich, C. Coletta, C. Chao, C. Szabo, The therapeutic potential of cystathionine β-synthetase/hydrogen sulfide inhibition in cancer, Antioxidants Redox Signal. 22 (2014) 424.
[30] L. Shen, Y. Cao, Z. Du, W. Zhao, K. Lin, L. Jiang, Illuminate the active sites of γ-FeOOH for low-temperature desulfurization, Appl. Surf. Sci. 425 (2017) 212.
[31] S. Lee, T. Lee, D. Kim, Adsorption of hydrogen sulfide from gas streams using the amorphous composite of α-FeOOH and activated carbon powder, Ind. Eng. Chem. Res. 56 (2017) 3116.
[32] Y. Li, W. Chen, Y. Qi, S. Wang, L. Li, W. Li, T. Xie, H. Zhu, Z. Tang, M. Zhou, $H_2S$-scavenged and activated iron oxide-hydroxide nanospindles for MRI-guided photothermal therapy and ferroptosis in colon cancer, Small 16 (2020) 2001356.
[33] A. Albanese, P.S. Tang, W.C.W. Chan, The effect of nanoparticle size, shape, and surface chemistry on biological systems, Annu. Rev. Biomed. Eng. 14 (2012) 1.
[34] D. Saliba, M. Ammar, M. Rammal, M. Al-Ghoul, M. Hmadeh, Crystal growth of ZIF-8, ZIF-67, and their mixed-metal derivatives, J. Am. Chem. Soc. 140 (2018) 1812.
[35] S. Tanaka, K. Fujita, Y. Miyake, M. Miyamoto, Y. Hasegawa, T. Makino, S. Van der Perre, J. Cousin Saint Remi, T. Van Assche, G.V. Baron, J.F.M. Denayer, Adsorption and diffusion phenomena in crystal size engineered ZIF-8 MOF, J. Phys. Chem. C 119 (2015) 28430.
[36] J.H. Cho, C. Lee, S.H. Hong, H.Y. Jang, S. Back, M.g. Seo, M. Lee, H.K. Min, Y. Choi, Y.J. Jang, S.H. Ahn, H.W. Jang, S.Y. Kim, Transition metal ion doping on ZIF-8 enhances the electrochemical $CO^2$ reduction reaction, Adv. Mater. 35 (2023) 2208224.
[37] H. Bunzen, Chemical stability of metal-organic frameworks for applications in drug delivery, ChemNanoMat 7 (2021) 998.
[38] J. Duan, B. Ma, F. Liu, S. Zhang, S. Wang, Y. Kong, M. Du, L. Han, J. Wang, Y. Sang, H. Liu, Coordination ability determined transition metal ions substitution of Tb in Tb-Asp fluorescent nanocrystals and a facile ions-detection approach, Nanoscale 10 (2018) 7526.
[39] D.J. Burleson, R.L. Penn, Two-step growth of goethite from ferrihydrite, Langmuir 22 (2006) 402.
[40] C. Frandsen, B.A. Legg, L.R. Comolli, H. Zhang, B. Gilbert, E. Johnson, J. F. Banfield, Aggregation-induced growth and transformation of β-FeOOH nanorods to micron-sized α-$Fe_2O_3$ spindles, CrystEngComm 16 (2014) 1451.
[41] Y. Wang, Z. Rong, X. Tang, S. Cao, X. Chen, W. Dang, L. Wu, The design of scorodite@FeOOH core-shell materials and its stability treatment for arsenide, Appl. Surf. Sci. 496 (2019) 143719.
[42] Y. Zhang, H. Chen, C. Guan, Y. Wu, C. Yang, Z. Shen, Q. Zou, Energy-saving synthesis of MOF-derived hierarchical and hollow $Co(VO_3)_2$-$Co(OH)_2$ composite leaf arrays for supercapacitor electrode materials, ACS Appl. Mater. Interfaces 10 (2018) 18440.
[43] C. Li, J. Ye, X. Yang, S. Liu, Z. Zhang, J. Wang, K. Zhang, J. Xu, Y. Fu, P. Yang, Fe/Mn bimetal-doped ZIF-8-Coated luminescent nanoparticles with Up/Downconversion dual-mode emission for tumor self-enhanced NIR-II imaging and catalytic therapy, ACS Nano 16 (2022) 18143.
[44] M. Zhang, H. Xue, J. Yang, X. Zhao, M. Xue, W. Sun, J. Qiu, Z. Zhu, Copper(ii)-based metal–organic framework delivery of calcium ascorbate for enhanced chemodynamic therapy via H2O2 self-supply and glutathione depletion, Biomater. Sci. 12 (2024) 1871.
[45] H. Jia, Q. Han, W. Luo, H. Cong, H. Deng, Sequence control of metals in MOF by coordination number precoding for electrocatalytic oxygen evolution, Chem Catal. 2 (2022) 84.
[46] L. Huang, X. Mao, J. Li, Q. Li, J. Shen, M. Liu, C. Fan, Y. Tian, Nanoparticle spikes enhance cellular uptake via regulating myosin IIA recruitment, ACS Nano 17 (2023) 9155.
[47] H. Yu, Y. Yu, R. Lin, M. Liu, Q. Zhou, M. Liu, L. Chen, W. Wang, A.A. Elzatahry, D. Zhao, Camouflaged virus-like-nanocarrier with a transformable rough surface for boosting drug delivery, Angew. Chem. 135 (2023) 202216188.
[48] X.B. Xiong, H. Uludağ, A. Lavasanifar, Virus-mimetic polymeric micelles for targeted siRNA delivery, Biomaterials 31 (2010) 5886.
[49] J. Chang, M. Han, Y. Wang, L. Wang, F. Lin, Q. Jia, J. Xu, W. Yang, G.a. Zhao, W. Ren, Z. Jin, Multifunctional iron oxide-hydroxide based nanorods for hydrogen sulfide scavenging assisted synergistic photothermal-chemotherapy of colon cancer, J. Sci. Adv. Mater. Devices 9 (2024) 100721.
[50] M. Fu, W. Zhang, L. Wu, G. Yang, H. Li, R. Wang, Hydrogen sulfide ($H_2S$) metabolism in mitochondria and its regulatory role in energy production, Proc. Natl. Acad. Sci. 109 (2012) 2943.
[51] K. Módis, Y. Ju, A. Ahmad, A.A. Untereiner, Z. Altaany, L. Wu, C. Szabo, R. Wang, S-Sulfhydration of ATP synthase by hydrogen sulfide stimulates mitochondrial bioenergetics, Pharmacol. Res. 113 (2016) 116.
[52] M. Milacic, D. Beavers, P. Conley, C. Gong, M. Gillespie, J. Griss, R. Haw, B. Jassal, L. Matthews, B. May, R. Petryszak, E. Ragueneau, K. Rothfels, C. Sevilla, V. Shamovsky, R. Stephan, K. Tiwari, T. Varusai, J. Weiser, A. Wright, G. Wu, L. Stein, H. Hermjakob, P. D'Eustachio, The reactome pathway knowledgebase 2024, Nucleic Acids Res. 52 (2023) 672.
[53] N. Liu, J. Zhu, W. Zhu, L. Chen, M. Li, J. Shen, M. Chen, Y. Wu, F. Pan, Z. Deng, Y. Liu, G. Yang, Z. Liu, Q. Chen, Y. Yang, X-ray-induced release of nitric oxide from hafnium-based nanoradiosensitizers for enhanced radio-immunotherapy, Adv. Mater. 35 (2023) 2302220.
[54] Y.k. Zhou, C.s. Han, Z.l. Zhu, P. Chen, Y.m. Wang, S. Lin, L.j. Chen, Z.m. Zhuang, Y. h. Zhou, R.l. Yang, M2 exosomes modified by hydrogen sulfide promoted bone regeneration by moesin mediated endocytosis, Bioact. Mater. 31 (2024) 192.
[55] Y. Chao, Z. Liu, Biomaterials tools to modulate the tumour microenvironment in immunotherapy, Nat. Rev. Bioeng. 1 (2023) 125.
[56] Y. Liu, L. Wang, X. Zhang, Y. Deng, L. Pan, H. Li, X. Shi, T. Wang, A novel cystathionine γ-lyase inhibitor, I194496, inhibits the growth and metastasis of human TNBC via downregulating multiple signaling pathways, Sci. Rep. 11 (2021) 8963.
[57] L. Huang, X. Li, H. Zhang, F. Liu, Z. Dai, F. Xiao, L. Wang, Z. Wang, Zinc ion-coordinated sericin calcium phosphate nanovaccines induce hyperactive dendritic cells and synergistic activation of T cells for cancer immunotherapy, ACS Nano 19 (2025) 13906.
[58] W.K.E. Ip, N. Hoshi, D.S. Shouval, S. Snapper, R. Medzhitov, Anti-inflammatory effect of IL-10 mediated by metabolic reprogramming of macrophages, Science 356 (2017) 513.
[59] E. Yang, X. Wang, Z. Gong, M. Yu, H. Wu, D. Zhang, Exosome-mediated metabolic reprogramming: the emerging role in tumor microenvironment remodeling and its influence on cancer progression, Signal Transduct. Targeted Ther. 5 (2020) 242.